Pore-scale multiphase flow modeling and imaging of CO_2 exsolution in Sandstone

Lin Zuo[a] Jonathan B. Ajo-Franklin[b] Marco Voltolini[b] Jil T. Geller[b] Sally M. Benson[a]

Abstract

This study utilizes synchrotron X-ray micro-tomography and pore scale modeling to investigate the process of gas exsolution and how it affects non-wetting phase relative permeability. Exsolved gas distributions are measured on Domengine and Boise sandstonesamples using synchrotron X-ray micro-tomography. Observed gas phase distributions are compared to a new model that simulates the growth and distribution of exsolved gas phase at the pore-scale. Water relative permeability curves are calculated using a Stokes flow simulator with modeled and observed gas distributions, under various conditions, such as rock geometry, and pressure depletion rates. By comparing the actual bubble distributions with modeled distributions, we conclude that exsolved gas is more likely to form and accumulate at locations with higher water velocities. This suggests that convective delivery of CO_2 to the gas bubble is a primary mechanism for bubble growth, as compared to diffusive transport through the aqueous phase. For carbonated brine flowing up a fault at half a meter per day, with 5% exsolved gas, the water relative permeability is estimated to be 0.6~0.8 for various sandstones. The reduction of water mobility reduces upward brine migration when even a small amount of exsolution occurs.

Keywords: CO_2 exsolution, Water mobility reduction, Relative permeability, Pore-scale Stokes flow

1. Introduction

Captured CO_2 injected into a geologic storage formation is expected to remain there for thousands of years or longer (Benson et al., 2005). However, a strong buoyancy force, caused by the lower CO_2 density with respect to brine, allows the CO_2 to move upward if an adequate seal is not present (Bachu et al., 1994, Pruess and Garcia, 2002, Pruess, 2005, Doughty, 2007, Nordbotten et al., 2008). Similarly, defects in the confining layer, such as seal-penetrating wellbores and faults, allow upward brine migration from the storage formation if a moderate upward pressure gradient exists due to groundwater extraction/irrigation or high CO_2 injection pressures (Oldenburg et al., 2012, Falta et al., 2013). Even intact cap rocks that prevent the CO_2 phase from leaking out of the storage reservoir may not prevent brine migration. Given the high solubility of CO_2 in brine, over time, the fraction of CO_2 dissolved in the brine phase will increase (McPherson and Cole, 2000, Perkins et al., 2005, Ennis-King and Paterson, 2005, Riaz et al., 2006). If CO_2saturated brine is transported upwards it will exsolve as the hydrostatic pressure declines. Understanding the fate and transport of exsolved CO_2 is needed to assess the risks associated with this possibility.

The process of CO_2 exsolution is analogous to the so-called solution gas drive process in an oil reservoir. Dissolved hydrocarbon gas can be released from oil when reservoir pressure drops during production. Experimental and modeling results show very low gas relative permeabilities (10^{-6}~10^{-3}) in gas/oil systems and large reductions in oil phase relative permeability under high pore pressures (Fishlock et al., 1988, Grattoni et al., 1998, Naylor et al., 2000, Poulsen et al.,, Tang and Firoozabadi, 2003) in sandstone and bead packs.

Carbon dioxide exsolution experiments conducted under conditions relevant to geological sequestration in sandstone show similarly large mobility reductions of both the CO_2 and water phases (Zuo et al., 2012, Zuo et al., 2013). The large impact of CO_2 exsolution on water flow has also been studied for improving water flooding efficiency in oil production(Alizadeh et al., 2011, Zuo and Benson, 2013).

Interestingly, studies of CO_2 supersaturated water injection for soil remediation do not demonstrate large mobility reductions for either the water or gas phase (Enouy et al., 2011, Fry et al., 1997). Fry et al. (1997) measured water relative permeability in a sand pack during exsolution that matched the van Genuchten-Mualem model calibrated by drainage data. Enouy et al. (2011) matched measured data in a sand pack with a Corey type function. They conclude that the gas phase moves by repeated mobilization, fragmentation and coalescence of large gas clusters (Zhao and Ioannidis, 2011).

Tsimpanogiannis and Yortsos (2002) propose a continuum model for the growth of a gas phase from a supersaturated liquid. They find the morphology and mobility of exsolved gas are controlled by nucleation and post-nucleation processes and are sensitive to the depletion rate. Tsimpanogiannis and Yortsos (2002) assume equilibrium at the liquid-gas interface and that mass transfer is controlled by solute diffusion. Pore network modeling studies of solution gas drive show that bubble generation and mobility are both strongly dependent on depletion rate and connectivity of the pore system (Nyre et al., 2008, Bondino,, Bondino et al., 2009).

In this paper, we obtain high-resolution images of exsolved CO_2 in two rock samples using synchrotron X-ray micro-tomography. Next we develop a bubble nucleation and growth algorithm to study the influence of depletion rate, nucleation fraction, rock geometry and mass transfer processes on the distribution and morphology of exsolved CO_2. Modeling results are then compared to synchrotron X-ray micro-tomography observations of bubble morphology. A Stokes flow simulator is used to calculate water relative permeability curves in the presence of exsolved CO_2 and understand the influence of CO_2 exsolution on subsurface flow under various conditions, including those most relevant to geological storage of CO_2.

2. Three-dimensional micro-tomography of CO_2 exsolution

Synchrotron X-ray micro-tomography allows direct observation of CO_2 exsolution in real rocks at the pore scale, albeit with some limitations on sample size, boundary conditions, and both temporal as well as spatial resolution. We present experimental results examining the dynamic distribution of CO_2 and brine for samples from two sandstone formations during exsolution, drainage, and imbibition. These data are used to compare differences between the distribution and morphology of the CO_2 introduced by these different mechanisms, as well as provide the basis for developing a mechanistic model of CO_2 exsolution and how it affects the transport properties of CO_2 and brine.

2.1. Materials

We conducted dynamic imaging experiments on Domengine and Boise sandstone samples as well as static characterization of a Berea sandstone core. The Domengine sample was obtained from a mine adit in Black Diamind Mine Regional Preserve (Contra Costa, CA); the Domengine formation is a regionally extensive high-permeability sandstone unit that is both exploited for commercial natural gas production and considered a potential target for geological carbon sequestration within the Sacramento Basin. The Domengine sample selected had weakly cemented sub-angular grains and occurred within a near-shore beach facies. The Boise and Berea cores were obtained from Kocurek Industries (www.kocurekindustries.com/boise-sandstone) and Cleveland Quarries(www.clevelandquarries.com/cores), were selected because of the extensive prior work conducted on these reference sandstones.

2.2. Equipment and data processing

Synchrotron X-ray micro-tomography imaging was carried out at Beamline 8.3.2. of the Advanced Light Source (ALS) over a three-day shift. Beamline 8.3.2 is an X-ray imaging facility suitable for the micro-structural characterization of geological specimens, with a good flexibility concerning sample size (up to 1.5 cm) and resolution (down to sub-micron). The Beamline, which operates on a superconducting bending magnet (11.5 keV critical energy) is described in detail by MacDowell et al. (2012). Recent studies at Beamline 8.3.2 have explored a variety of problems related to the pore-scale coupling of structure, hydrogeology, and geochemistry (Wu et al., 2011, Armstrong and Ajo-Franklin,, Noiriel et al., 2012, Landrot et al., 2012, Kneafsey et al., 2013). As with all imaging techniques, a field of view versus resolution tradeoff needs to be addressed, thus limiting the sample size observable at a given voxel size. In the case of clean sandstones, as in the present work, a voxel size of 4.4 μm allows a proper description of the vast majority of the objects in the sample. Also, a temporal resolution linked to the dataset acquisition limits the temporal resolution. Because of the significant vertical length of the sample in comparison to the field of view, it was scanned as a sequence of 3 tiled acquisition runs with a small amount of overlap; additionally, only the middle section of each sample was imaged.

Acquisition of each tile required 1441 angular projections and 240 ms exposure time per projection, with interleaved flat field images acquired to correct for temporal variations in beam structure. Raw projections were corrected for dark current and flat field variations followed by denoising (median filter) and ring removal. The reconstruction of the volumes was carried out by using conventional filtered back projection (Octopus, inCT), after applying single-distance phase retrieval algorithm (Paganin et al., 2002) to the projections using the software ANKAPhase (Weitkamp et al., 2011). This procedure mitigates the phase-contrast artifacts and improves the greyvalue contrast among the different phases, aiding with the segmentation process.

2.3. Experimental procedure

Carbon dioxide and brine (degassed deionized water with 1 mol/L potassium iodide) were used as the gas and aqueous phases. Sandstone samples were prepared as cylindrical cores, 8 mm in diameter and 15~20 mm in length. The cylindrical surface was coated with Epoxy resin, wrapped in a shrinkable Teflon sleeve and mounted vertically on a rotary stage in the chamber of Beamline 8.3.2. Spirals of flexible tubing were connected to inlet and outlet of the sample, to allow ease of rotation tension during scanning. The experimental configuration (Fig. 1) consists of two syringe pumps (Teledyne Isco, Model 100DM) and a CO_2-water mixing vessel..

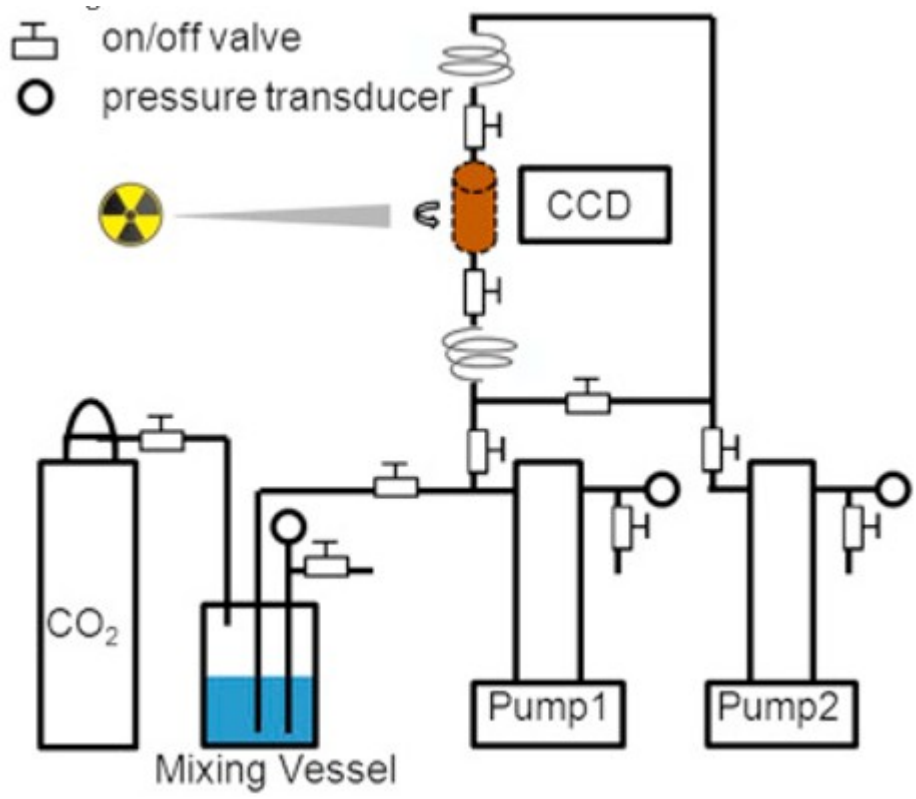

Fig. 1. Schematic of micro-tomography experiment setup.

A baseline scan of the dry sample was acquired before injecting brine into the core. The pore pressure was then increased to 584 kPa. CO_2 and brine were mixed in the mixing vessel at 584 kPa for one hour to reach equilibrium. Then, pump#1 was drained, refilled with carbonated brine from the mixing vessel, and used to flush the carbonated brine through the sample at 618 kPa. A baseline scan of the carbonated brine saturated sample was acquired to ensure good phase contrast and complete removal of residual air in the sample. Pore pressure was reduced at a rate of 1000–2000 kPa/h by withdrawing fluids from both ends of the sample to Pump#2. Scans were taken when the pore pressure declined to 377 and 274 kPa. The CO_2 distributions from drainage and post-drainage imbibition were also acquired at 618 kPa with injection rates of 0.1 mL/min CO_2 (Ca $\approx 10-8$) or brine (Ca $\approx 7\times10-7$). All experiments were conducted at ambient temperature.

The sample rotates 180° for acquiring images of a desired volume. Four hours are required to finish imaging a 5 mm length section of the sample at a resolution of 4.4 μm. After volume reconstruction of raw projections, a manual segmentation was performed to separate the three different phases: sand matrix, brine, and CO_2(gas). One reconstructed slice of the Domengine sample after CO_2 exsolution is shown in Fig. 2 with its grey-level histogram. The three phases are well separated and the associated peaks are visible in the grey-scale plot. Outliers are feldspar and high-density minerals that display higher grey values..

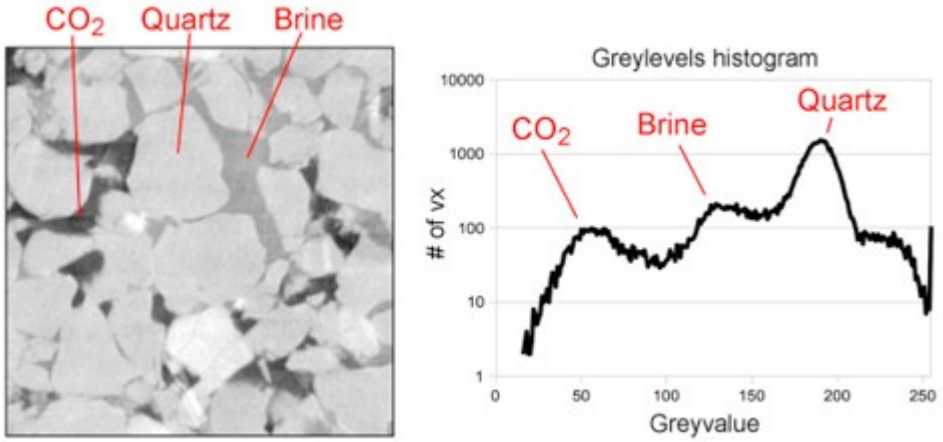

Fig. 2. A slice image of the Domengine sample with exsolved CO_2 (left) and its greylevel histogram (right).

2.4. Experimental results

Three-dimensional CO_2 distribution volumes were generated for the Domengine sandstone and the Boise sandstone during identical drainage, imbibition and exsolution processes (Fig. 3). Each individual CO_2 ganglion is labeled a different color from its neighbors to allow visualization of gas phase connectivity. During drainage, a connected gas phase forms in both samples, reaching a 54% gas saturation in the Domengine sandstone and 24% in the

Boise sandstone. During imbibition, residual trapping is significantly different in the two samples. Almost no gas is trapped (2%) in the Domengine sandstone. For the Boise sandstone, the injected brine bypasses large portions of gas-filled pore space, leaving a residual gas saturation of about 15%. During exsolution, individual gas ganglia spanning multiple pores develop in the Domengine sandstone. Most of the exsolved gas in the Boise sandstone is confined to single pores when pore pressure drops to 377 kPa. When the pore pressure is further reduced to 274 kPa, the exsolved gas saturation increases from 16% to 49% in the Domengine sandstone and 9–19% in the Boise sandstone. Fig. 4 shows exsolved gas ganglion size distributions at 377 and 274 kPa for comparison. Data from the Domengine sandstone show that the ganglion size distribution is independent of pressure or gas saturation. For the Boise sandstone, reduction of median size ganglia and increase the proportion of large and small size ganglia (at the expense of mid-size ganglia) suggest that snap-off and aggregation occur while the pressure drops from 377 to 274 kPa...

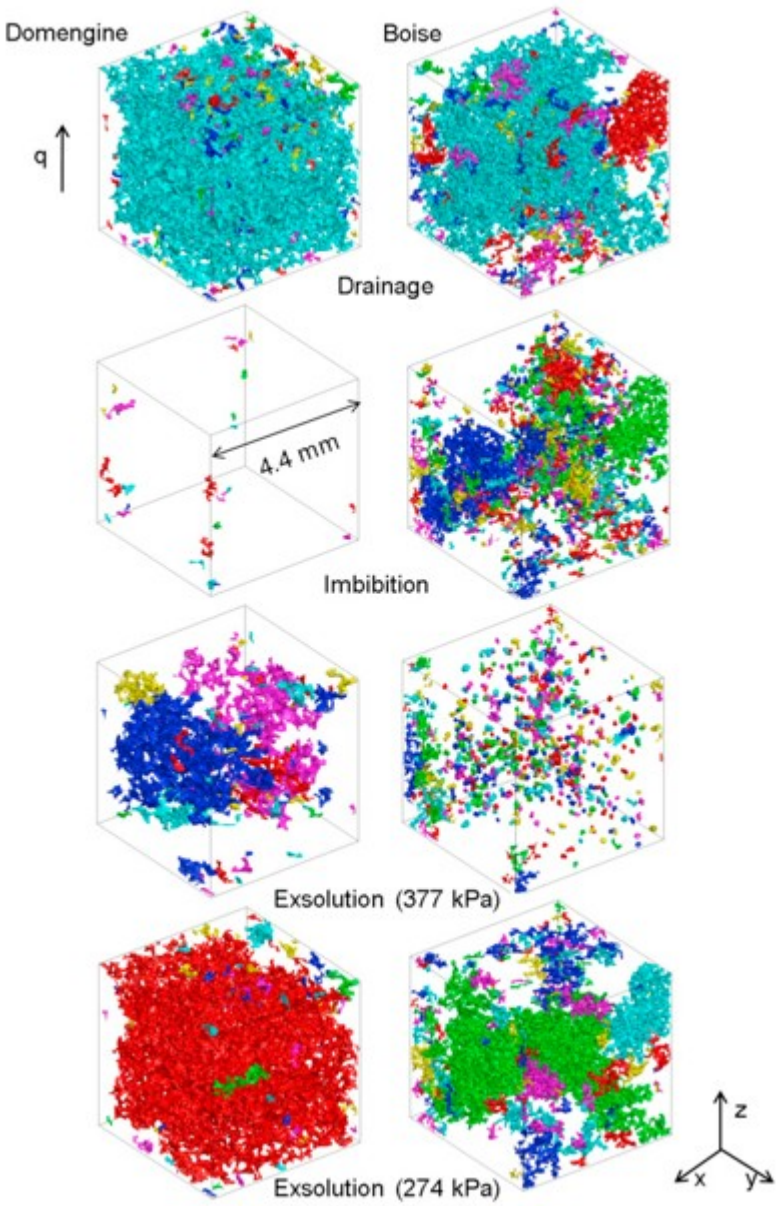

Fig. 3. Three-dimensional visualizations of CO_2 in the Domengine and Boise sandstones.

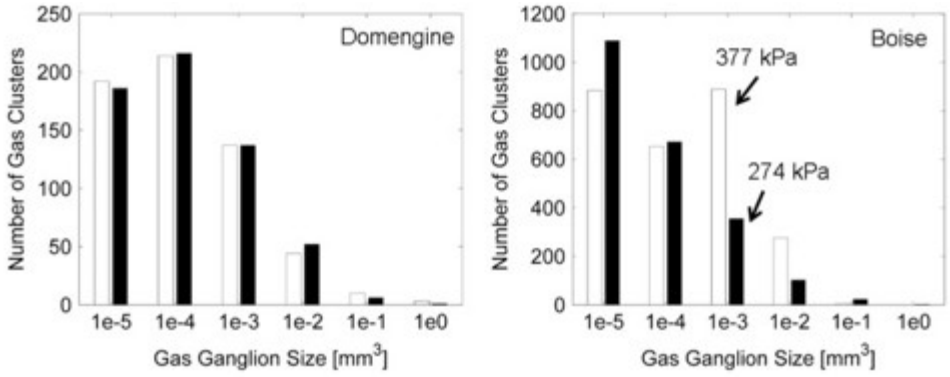

Fig. 4. Ganglion distributions of exsolved CO_2 in the Domengine and Boise sandstones.

Given that all experimental conditions and procedures are identical between the two samples, differences between the gas phase distributions must arise from the differences in pore-scale geometry. Fig. 5 shows digitally reconstructed cross sections of the Domengine and Boise sandstones. From the inspection of the data, it is possible to visually appreciate the larger pore size of the Domengine sandstone with respect to the Boise sandstone. For the same saturation, capillary pressures will be higher in the Boise sandstone. The pore space morphology in the Boise sandstone is also more conducive to snap-off, as supported by the higher degree of trapping observed during imbibition (Tanino and Blunt, 2012)..

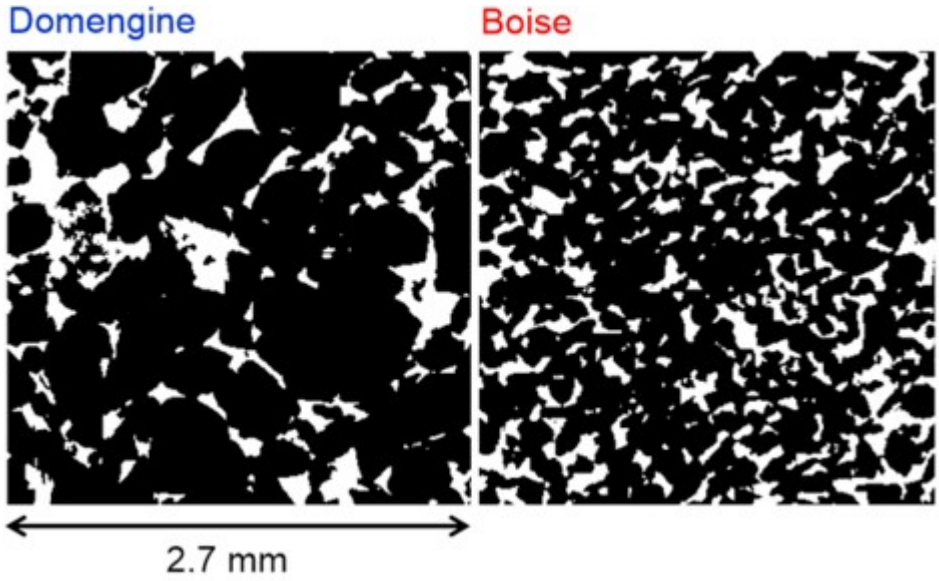

Fig. 5. Cross sections of the Domengine and Boise sandstones.

While it is reasonable to assume that nucleation sites are randomly distributed on the grain surfaces of a volume of hundreds of pores and nuclei can appear anywhere, nuclei grow by diffusive and convective mass transfer and they compete for the available solute in the aqueous phase (Du and Yortsos, 1999). Consequently, it is possible that nuclei exhibit preferential growth in ganglia with the lowest capillary pressures. These are likely to be in the largest pores. In addition or as an alternative, preferential bubble growth could occur in pores with the highest convection rates. Micro-tomographic imaging combined with Stokes flow simulation of aqueous velocity distributions allows examination of these hypotheses in greater detail.

Fig. 6 shows probabilities of observing exsolved gas at 377 kPa in the Domengine and Boise sandstones with different pore size (left) and aqueous velocities (right) in the pore space. Fig. 7 provides the same data at 274 kPa. In these figures, sampling voxels are centers of ellipses fit to individual pores. The corresponding voxel velocity is obtained from a velocity distribution calculated by a Stokes flow simulation code (Appendix A) in reconstructed digital rock volumes without exsolved gas and is normalized

by the maximum velocity in each corresponding velocity distribution. Exsolved gas is evenly distributed among different pore sizes in both the Domengine and Boise sandstones. The probability of observing a gas bubble increases linearly with increasing velocity for both rock samples at 377 kPa. Similarly, a linear relationship is observed for the Boise sandstone at 274 kPa. However, for the Domengine, by the time the pressure drops to 274 kPa, the saturation has increased to 49% and there is no correlation with either pore size or velocity. Note that in both samples, there is less than 5% of pore space that has a velocity larger than 0.5 (normalized by the maximum velocity in the sample) and this consists of the most important pores and throats that influence fluid flow and determine permeability of the entire sample...

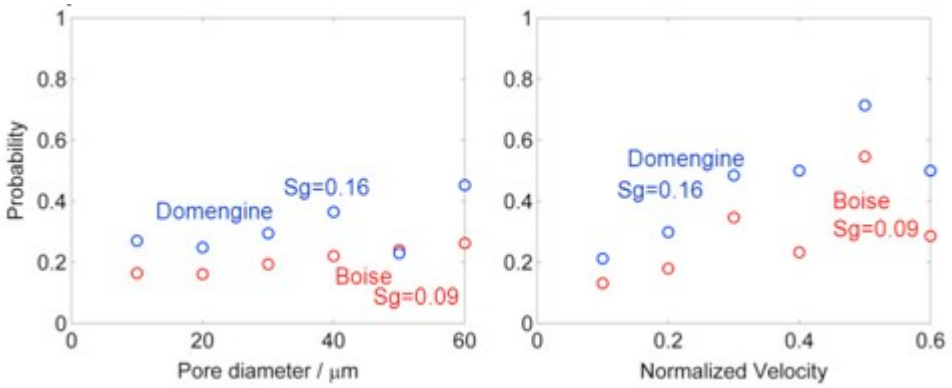

Fig. 6. Probability of observing exsolved CO_2 with different pore size (left) and flow velocities (right) at 377 kPa.

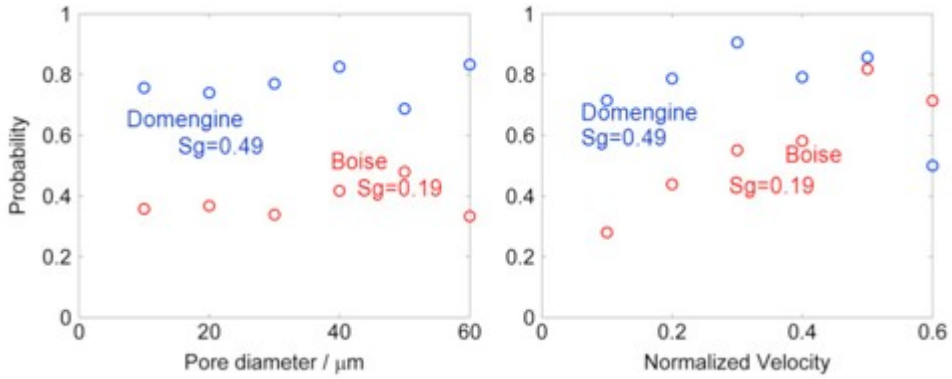

Fig. 7. Probability of observing exsolved CO_2 with different pore size (left) and flow velocities (right) at 274 kPa.

The good correlation between aqueous phase velocity and the presence of exsolved gas suggests that convective mass transfer plays an important role in bubble growth during the early stages of exsolution. This observation also helps explain why the presence of a small amount of exsolved CO_2 can dramatically reduce the permeability to the aqueous phase as has been observed in core-scale experiments (Zuo et al., 2012, Zuo et al., 2013). The exsolved gas bubble preferentially growth in the most important pathways

for aqueous flow, and consequently reduce the aqueous phase mobility by plugging the pore spaces.

In the following section we develop a coupled bubble growth and stokes flow simulator to compare to the observed gas distributions under laboratory conditions. Then, we will study the influence of depletion rate, nucleation fraction, rock geometry and mass transfer processes on the distribution and morphology of exsolved CO_2 and understand the influence of CO_2 exsolution on subsurface flow under conditions most relevant to geological storage of CO_2.

3. Gas nucleation and growth modeling

3.1. Theories and methods

When pressure decreases, transient gas nuclei appear by thermal fluctuations (Scriven, 1959, Wilt, 1986). The nucleus is stable only if its size or the pressure inside is large enough to prevent collapse under the force of capillary pressure. Firoozabadi and Kashchiev (1996)assume that all bubbles nucleate at the same time at randomly located active nucleationsites. Yortsos and his coworkers (Yortsos and Parlar, 1989, Satic et al., 1995, Li and Yortsos, 1995) propose another theory for a porous medium with slow rates of pressure decline, which postulates various sites on solid surfaces become activated progressively. They also conclude the nucleation fraction, the fraction of pores ultimately activated, is a power law of the pressure decline rate. Experimental observations and modeling results show that although nucleation occurs progressively, it is instantaneous compared to the long depletion time (El-Yousfi et al., 1997, Arora and Kovscek, 2003).

Individual bubbles grow by diffusion through the aqueous phase and mass transfer into the gas phase. As the bubble grows, capillary pressure will increase when the liquid-gas interface penetrates into pore throats. When the capillary threshold at the throats is overcome, the bubble will expand into neighboring pores. Thus, the distribution and morphology of exsolved gas in the pore space is largely affected by capillary pressure.

Although nucleation initiates at crevices, cavities and pre-existing micro bubbles, we cannot literally model such nucleation processes in any representative volume of a real rock. Even if we could, these nuclei do not have a significant influence on fluid flow unless they grow to the size comparable to a pore. The important question is where the exsolved gas accumulates under the constraints of mass transfer, capillarity, and pore geometry such that fluid flow in the porous medium is affected.

Thus, in our model we assume nucleation sites are randomly distributed on grain surfaces and that the nucleation process is instantaneous. Here we consider two conceptual scenarios for the post-nucleation bubble growth: (1) bubble growth at each nucleation site is unaffected by bubble growth in nearby pores resulting in simultaneous growth of bubbles in proportion to their surface area, referred to as the diffusion-controlled scenario; (2)

bubbles in regions with high convective brine flows grow preferentially until their capillary pressure is equal to or higher than nearby bubbles, at which time the bubbles with lower capillary pressure begin to grow, referred to as the transport-enhanced scenario.

Illustrations of these two scenarios are shown in Fig. 8. Consider two bubbles, *i* and *j*, which initiate at t_0 and grow to the same radius at t_1. In the diffusion-controlled scenario, we assume diffusion of dissolved CO_2 in the surrounding liquid is always sufficient to support the growth of individual bubbles so the growth of bubble *i* and *j* is not affected by each other (Fig. 8, left). Thus, each bubble has its own capillary pressure controlled by the local pore geometry. Bubble *i* and *j* grow simultaneous from t_1 to t_4. In the transport-enhanced scenario, we assume diffusion of dissolved CO_2 in the surrounding liquid is not sufficient to support the growth of all bubbles thus bubbles formed in high flux locations grow preferentially. Also, we assume the transport of CO_2 molecules in the aqueous phase is so fast that bubbles with the lowest capillary pressure grow first. In this scenario, assume bubble *i* and *j* start in high flux locations and grow to the same radius at t_1. Since bubble *i*resides in a bigger pore that allows it to grow with a lower capillary pressure, it grows from $t_1$to t_4 while bubble *j* remains the same size (Fig. 8, right)..

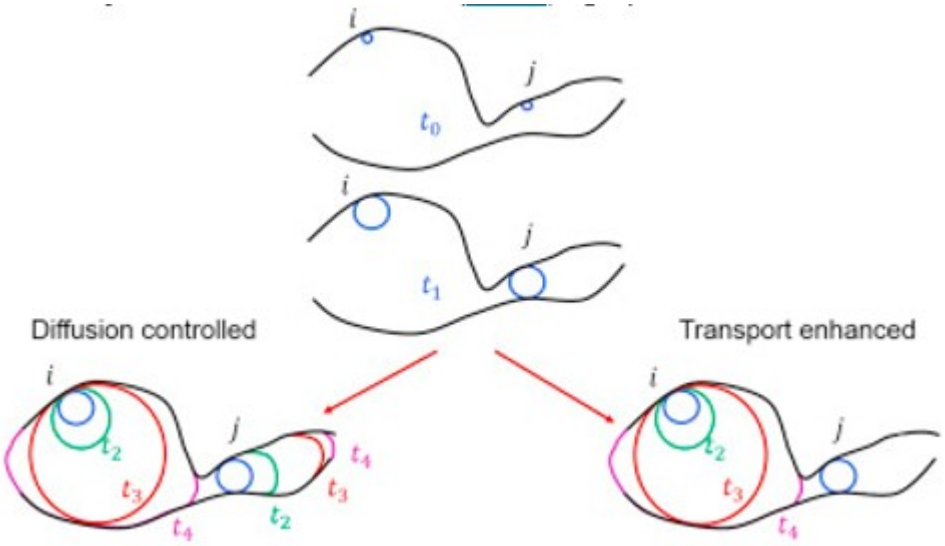

Fig. 8. Illustrations of gas growth in the diffusion-controlled scenario versus the transport-enhanced scenario.

The bubble nucleation and growth model is formulated as shown in Fig. 9: first, nucleation sites are randomly selected until a specified number of activated nucleation sites are located. In the diffusion-controlled scenario, randomization is surface area weighted, i.e. a certain fraction of pore surface voxels are selected as nuclei. In the transport-enhanced scenario, randomization is velocity weighted, i.e. voxels with large velocities have higher chances to be selected as nuclei. This takes into account the preferential growth of bubbles at high flux locations in the transport-

enhanced scenario, because nuclei in unfavorable locations will not grow. As a result, we compare the two scenarios with the same numbers of active nuclei..

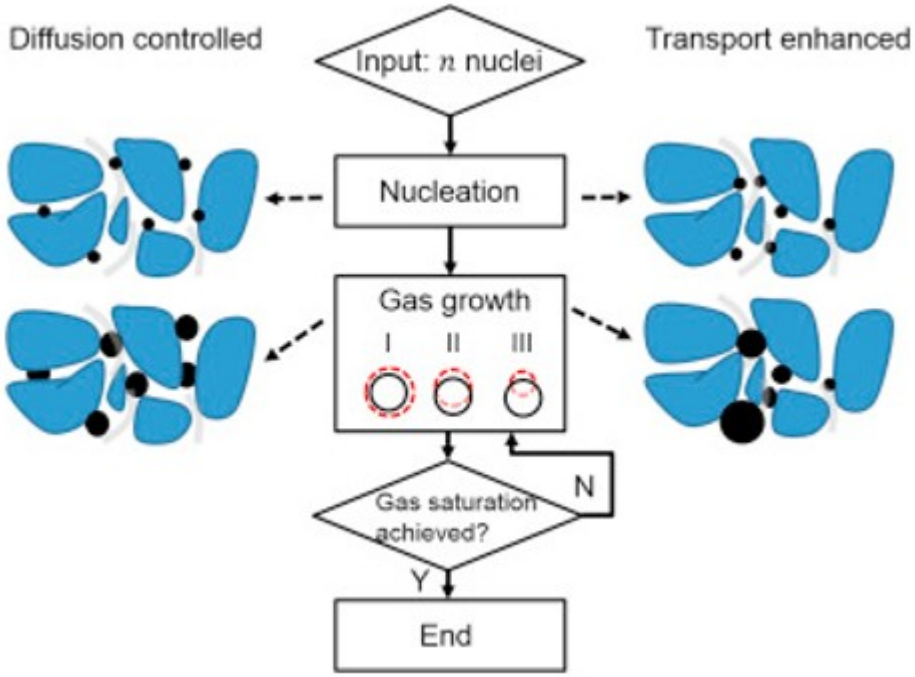

Fig. 9. Flow chart of the bubble nucleation and growth model and illustrations of the diffusion-controlled scenario versus the transport-enhanced scenario.

In the model, interfaces of individual bubbles consist of spherical surfaces with different radii. For example, after nucleation, nuclei are described as spheres with zero radii. A bubble, conformed in an irregular pore, has a gas-liquid interface that can be described by a set of centers, {c¯}, and their corresponding radii {r}. Since the bubble grows in the way of minimizing capillary pressure, only the surfaces associated with the largest radius, or the active radius r_a, can expand, while the inactive surfaces (associated with inactive radii {ri}and inactive centers {c¯i}) remain static.

When a bubble expands, there are three scenarios: I. pure expansion; II. elongation without change of curvature; and III. elongation with increase of curvature (‘Gas Growth’ in Fig. 9). The active surfaces of a bubble expand through modifications of the active radius r_a and the active centers {c¯a} as described in the following algorithm:

First, an attempt is made to update the active radius to ra+1 with the original active centers (Scenario I); if all expanded surfaces intersect grain surfaces, attempts are made to search the adjacent voxels (26-connected neighborhood in three dimensional space) of each active center with the original active radius (Scenario II); if still none of the searches yield an expanded surface without intersecting grain surfaces, the final attempts are made: (Scenario III) the adjacent voxels of each active center are searched

with reduced radius, ra−1. This step increases the capillary pressure of a growing bubble to overcome pore throats.

In each iteration, the growth of a bubble completes as the expanded surfaces are determined and the active radius/centers are updated. Volumetric grow rate is proportional to the expanded surface area, i.e. $\Delta V \approx \sum\{c^{-}a\}(ra)2$.

Now we consider multiple bubbles. In the diffusion-controlled scenario, each bubble expands with its active surfaces, unaffected by bubble growth in nearby pores. Each bubble has an active radius that determines its capillary pressure. In the transport-enhanced scenario, active radii of all bubbles are compared, and only the bubbles with the maximum active radius are allowed to expand.

After nucleation sites are randomly selected in a porous medium, the model progresses by iterations of active bubble screening, active surface screening and surface expansion, until a specified gas saturation is achieved. Although the proposed model is simplistic in many ways and assumes uniform water-wet surface in the rock, it can be used to understand the influence of depletion rate, pore geometry and convective transfer on the formation and mobility of exsolved gas during exsolution.

3.2. Modeling results

The bubble nucleation and growth model is used to simulate gas growth in a two-dimensional micromodel (Zuo et al., 2013) and in digitally imaged pore spaces of Domengine, Boise and Berea sandstones. We first demonstrate modeling bubble growth under capillarity in the two-dimensional micromodel. Then, we simulate gas distribution and morphology in three-dimensional pore structures, and discuss the influence of nucleation fraction and pore geometry on gas growth in both the diffusion-controlled and transport-enhanced scenarios.

Fig. 10 shows modeling of gas exsolution in a micromodel and compares it to an experimental observation (right) (Zuo et al., 2013). By taking a sequence of images during pore pressure depletion and superimposing them sequentially, the evolution of a nucleus can be mapped over a period of time. The resultant image (right) has grains in maroon (immobile), the aqueous phase in blue, and the exsolved CO_2 phase in a color intensity, indicating how many times a gas phase is identified at the same location in the sequence. Modeling gas evolution is straightforward by initiating nuclei at locations where the bubble first appears. However, an exact nucleation location is not important for modeling gas ganglia spanning several pores since the host pore will be occupied first no matter where the nucleus initiates and the further evolution of gas topology is governed by capillary pressure only. Here we only model the growth of one bubble observed at the center (Fig. 10, right). The modeled result (left) demonstrates the

progressive growth of this bubble under capillarity and matches well with the observation..

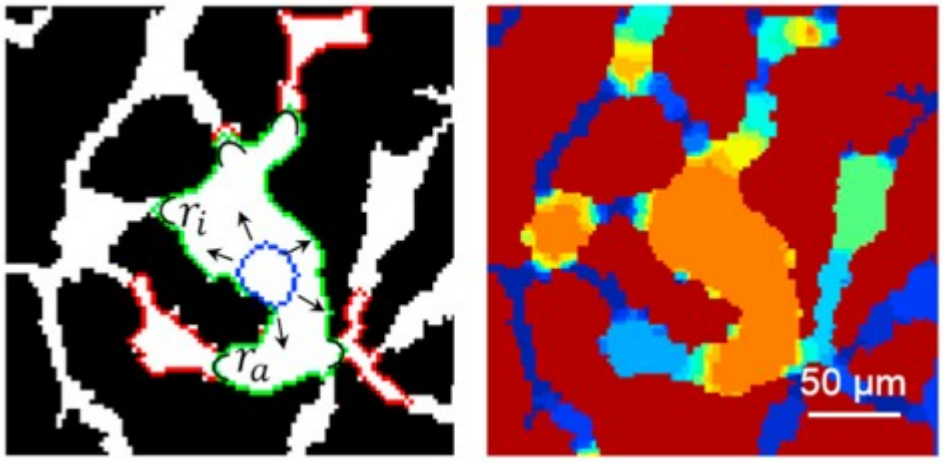

Fig. 10. 2D modeling of gas exsolution and comparison to experimental observation in a micromodel (right) (Zuo et al., 2013).

For modeling bubble nucleation and growth, one variable in the model is the number of activated nucleation sites, *n*. By setting *n*=1 and the nucleation location on the inlet boundary of a digital rock volume, we are able to model a gas finger during drainage, where injected gas invades pores with largest pore throats and travels through the porous medium in a connected ganglion (Fig. 11, left). In this way, the model is similar to the Maximum Inscribed Sphere method which extracts the geometry and connectivity of pore space (Al-Raoush and Willson, 2005, Silin and Patzek, 2006, Dong and Blunt, 2009) to determine gas distribution, flow and trapping in drainage/imbibition processes. If more than one nucleus is activated, n>1, inside the porous medium, gas exsolution can be modeled (Fig. 11, right) and the result shows that the same amount of gas is distributed more uniformly and dispersedly than an otherwise connected gas phase in drainage, similar to a residual gas phase..

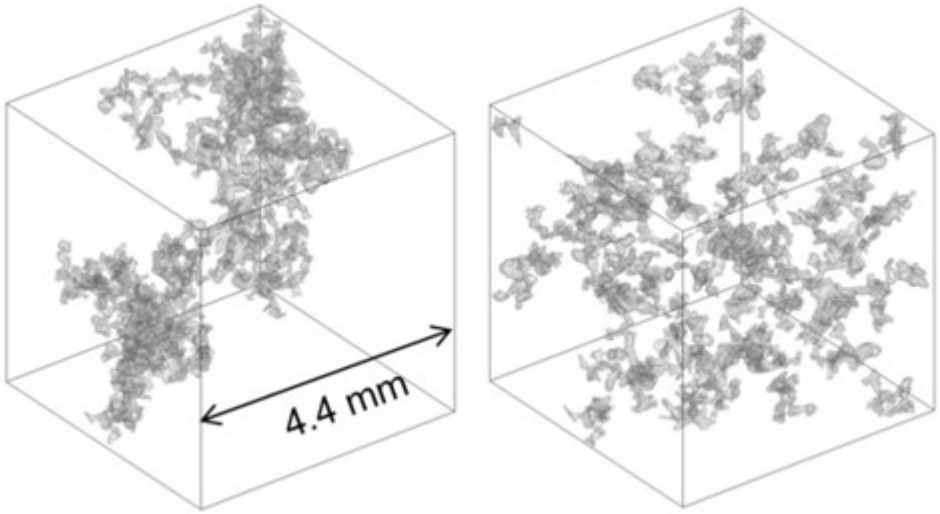

Fig. 11. Modeling of CO_2 distribution and connectivity in the Domengine sandstone. 1 nucleus (left) versus 100 nuclei (right) at 15% gas saturation.

Now we perform gas nucleation and growth modeling in digital volumes acquired from Domengine and Boise sandstone samples. Data acquisition and processing of the rock images are discussed in detail in Section 2. Fig. 12, Fig. 13 show the modeled exsolved CO_2distributions (15%) in the Domengine and Boise sandstones for comparison. Modeled distributions are compared for the diffusion-controlled scenario and the transport-enhanced scenario with same nucleation fractions, ranging from 10^{-6} to 10^{-3}. Here the nucleation fraction is defined as the number of activated nuclei per unit grain surface area. Generally, exsolved gas ganglia have a smaller average size and are less connected as the nucleation fraction increases. The difference between the two scenarios is that the transport-enhanced gas size distribution is less sensitive to the nucleation fraction. Since there are limited transport-enhanced locations in a porous medium, only certain numbers of activated nuclei can grow, thus there are fewer ganglia in the transport-enhanced case and the size distribution is more variable...

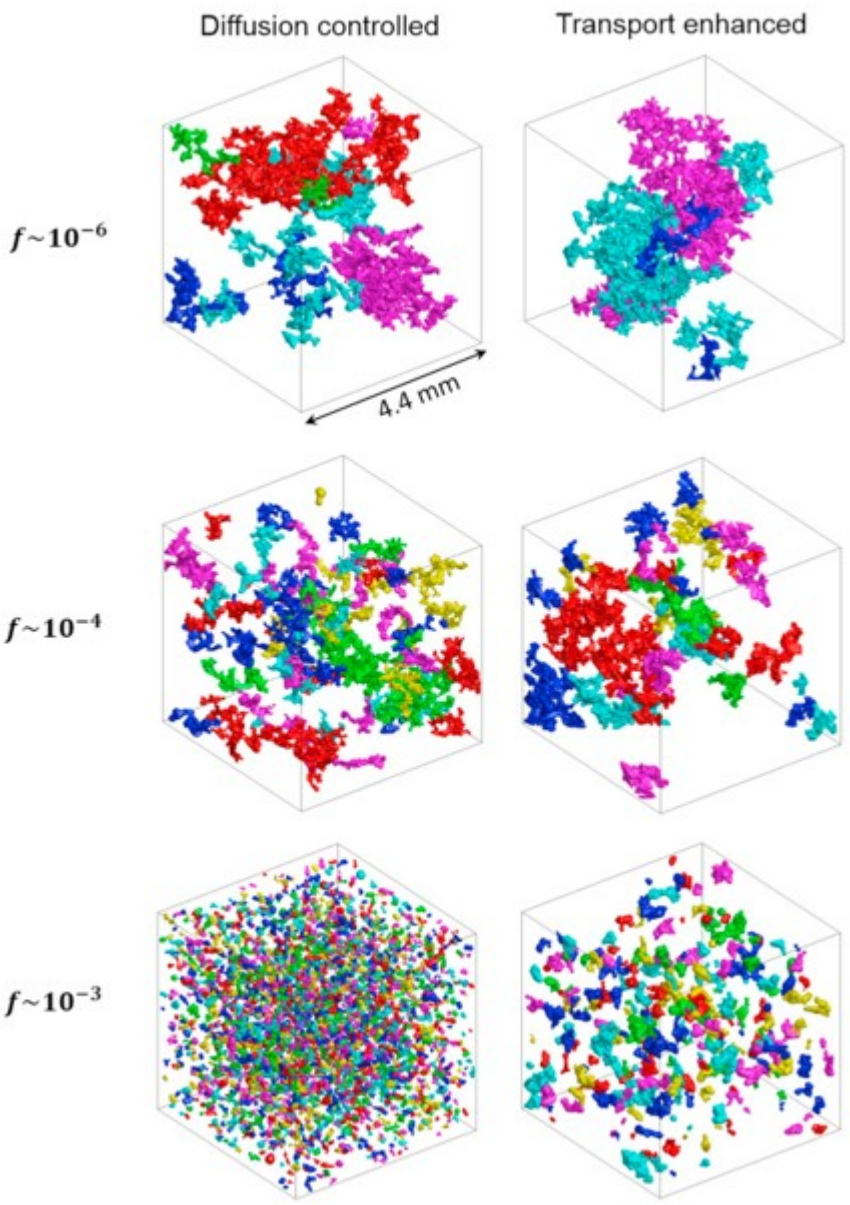

Fig. 12. Modeling of gas exsolution in the Domengine sandstone with different nucleation fractions. 15% gas saturation in both the diffusion-controlled scenario (left) and the transport-enhanced scenario (right).

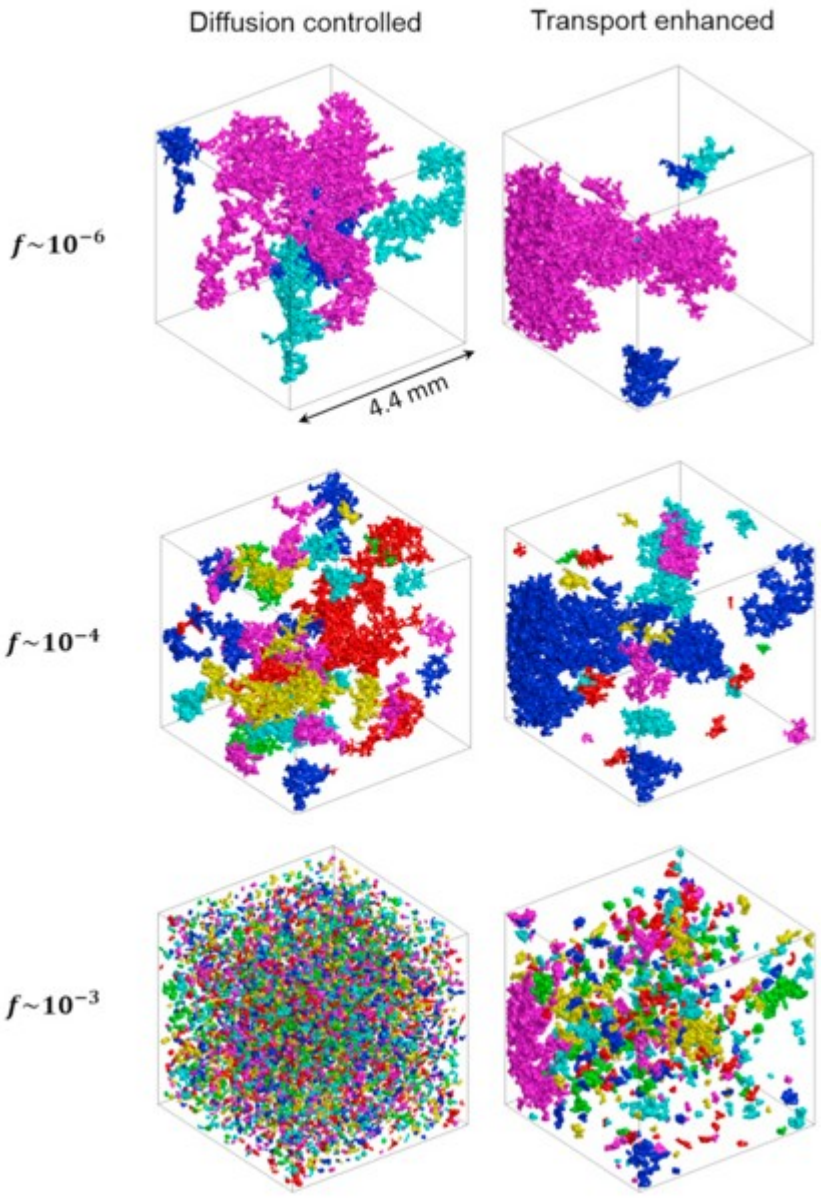

Fig. 13. Modeling of gas exsolution in the Boise sandstone with different nucleation fractions. 15% gas saturation in both the diffusion-controlled scenario (left) and the transport-enhanced scenario (right).

Fig. 14, Fig. 15 compare modeled (shaded) and experimental (bars) ganglion size distributions of exsolved CO_2 in the Domengine and Boise sandstones. The ganglion size is defined as the voxel volume occupied by a ganglion. For the modeled ganglion distributions, the size of ganglia reduces as the nucleation fraction increases in all cases. While most ganglia have similar sizes in the diffusion-controlled scenario with each nucleation fraction, variations of modeled ganglia size in the transport-enhanced scenario is larger and match the experimental observations better. Both visual and statistical comparisons between modeled gas distributions and experimental observations suggest that post-nucleation gas growth is enhanced by

convective transfer in the aqueous phase. It is also consistent with experimental data shown in Fig. 6, Fig. 7. Modeled distributions at 10^{-3} nucleation fraction appear to match experimental observations in both sandstones...

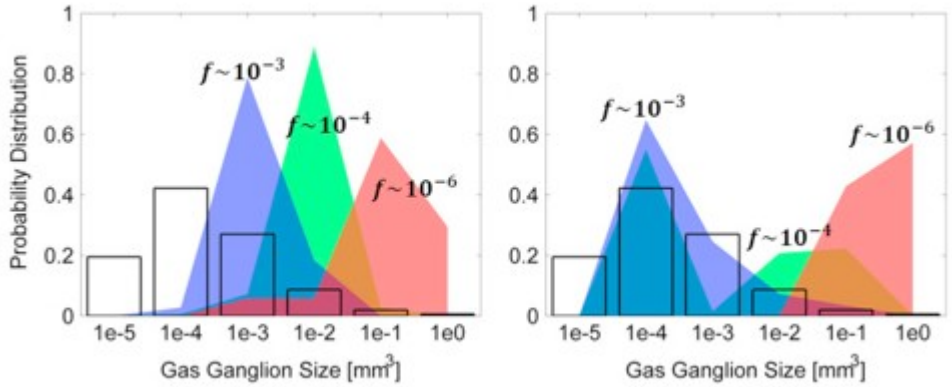

Fig. 14. Comparison of modeled (shades) and experimental (bars) ganglion size distributions of exsolved CO_2 in the Domengine sandstone in the diffusion-controlled (left) and convection-controlled (right) scenario.

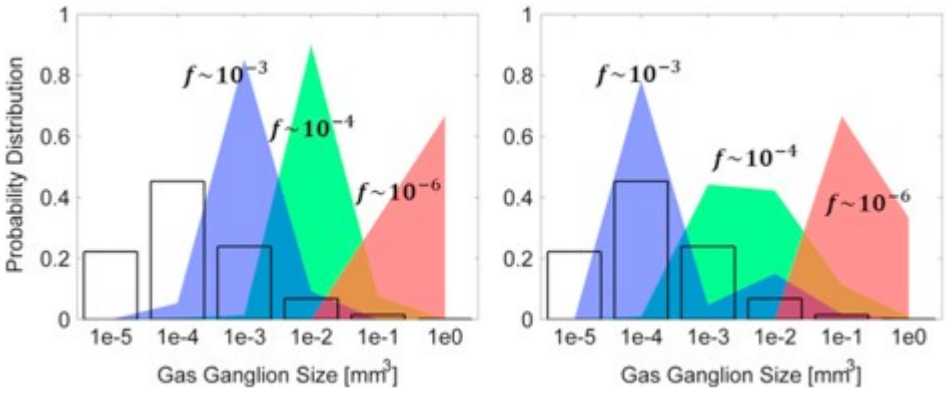

Fig. 15. Comparison of modeled (shades) and experimental (bars) ganglion size distributions of exsolved CO_2 in the Boise sandstone in the diffusion-controlled (left) and convection-controlled (right) scenario.

4. Relative permeability simulations

We have developed a bubble nucleation and growth model in porous media that replicates the gas distribution and morphology observed in our experiments. The availability of statistically realistic gas distributions allows exploration of the implications of their impact on the relative permeability to water. We now present an approach for estimating water relative permeability curves with modeled CO_2 distributions under various reservoir conditions using a numerical Stokes flow simulation.

4.1. Simulated relative permeability curves

We now use generated exsolved CO_2 distributions in the rock volumes to calculate velocity distributions and wetting phase relative permeability with a Stokes flow simulator (Appendix A). The influence of exsolved CO_2 on fluid flow can be seen on Fig. 16. Isosurfaces of normalized velocity are colored to

highlight the pore connections and high velocity pathways (blue/green/red: 10/50/80% of maximum velocity) in a portion of the Domengine sandstonewithout exsolved gas (Fig. 16, right). The effect of the presence of exsolved CO_2 (grey) under the same pressure differential (Fig. 16, left) clearly demonstrates that the exsolved CO_2 clogs some flow paths and reduces the overall flow. Comparison of velocity vectors in Fig. 17 clearly shows the influence of exsolved CO_2 on fluid flow...

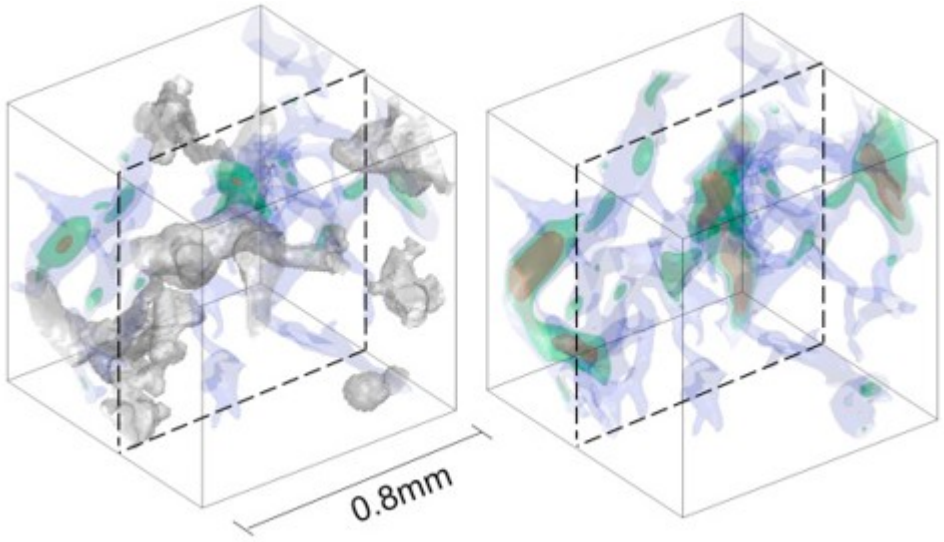

Fig. 16. Isosurfaces of simulated velocity fields in a portion of the Domengine sandstone sample, with (left) and without (right) exsolution.

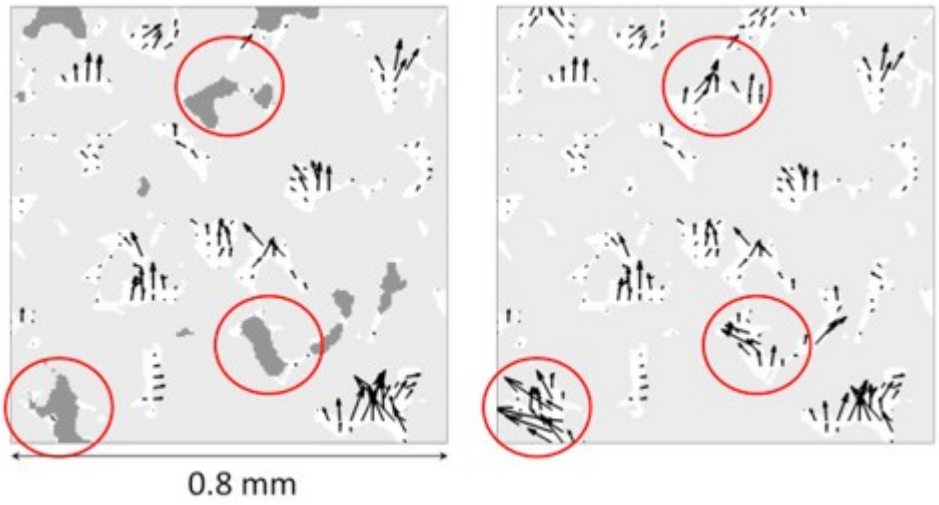

Fig. 17. Quiver plot of simulated velocity vectors in a vertical slice of the Domengine sandstone sample, w/(left) and w/o (right) exsolved CO_2 (dark grey).

We estimate water relative permeability curves with the presence of exsolved CO_2 as follows: (1) calculate the absolute permeability of a rock volume without gas; (2) generate realizations of exsolved CO_2 distributions in the rock volume up to 35% gas saturation (10 realizations with each

nucleation fraction); (3) calculate the effective permeabilities of the rock volume with 5%, 15%, 25% and 35% gas saturations for each realization.

Fig. 18 shows the calculated water relative permeability curves in the diffusion-controlled scenario for the Domengine sandstone (blue), Boise sandstone (red) and Berea sandstone (green). Curves with two nucleation fractions (10^{-2} and 10^{-6}) are shown for each sandstone. Each shaded area represents the variation of calculated relative permeability values of ten realizations (average value±one standard deviation). Generally, as the nucleation fraction increases, more but smaller ganglia evolve in the rock volume, and the flow of water is further hindered by the higher possibility of gas ganglia blocking flow paths under the same gas saturations. Also, variations (or uncertainties) of calculated water relative permeabilities among realizations is reduced as the nucleation fraction increases, indicating a similar gas morphology will form regardless where nuclei initiate if the nucleation fraction is large enough. The general trend also applies for the transport-enhanced scenario..

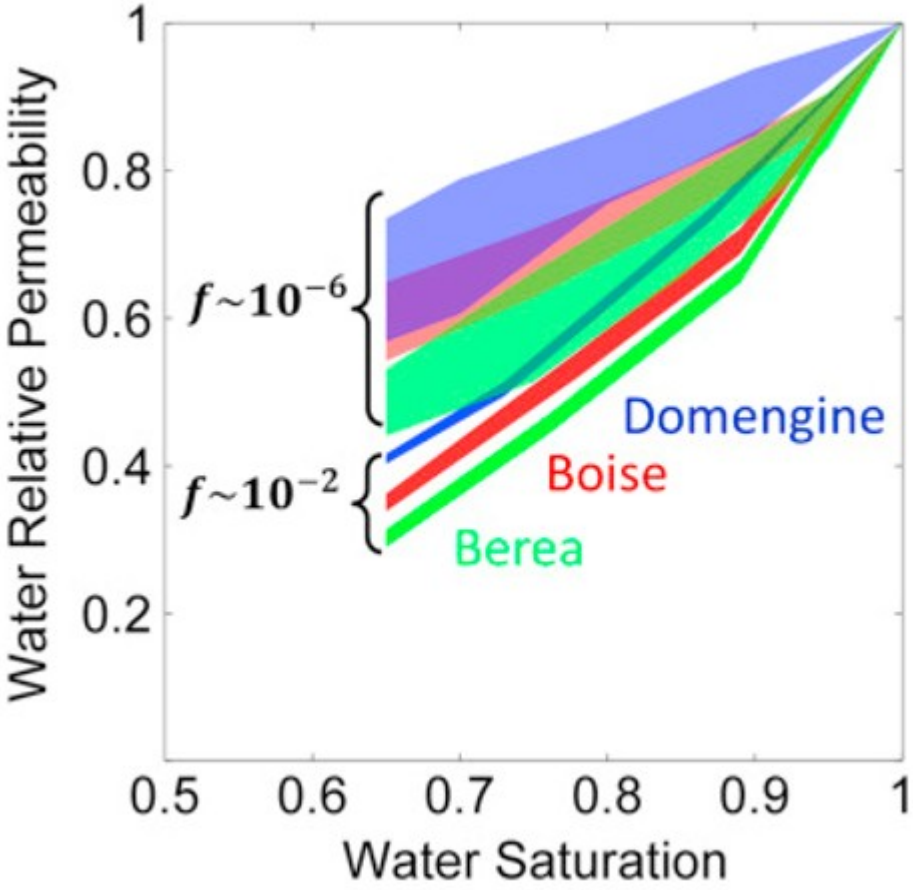

Fig. 18. Variations of calculated water relative permeability curves at different nucleation fractions in the diffusion-controlled scenario. Shaded area represents average value±one standard deviation of ten gas distribution realizations (Domengine sandstone: blue; Boise sandstone: red; Berea sandstone: green).

Fig. 19 compares water relative permeability curves between the diffusion-controlled scenario (w/o markers) and the transport-enhanced scenario (w/ markers), for the Domengine sandstone (blue), Boise sandstone (red) and Berea sandstone (green). Calculated curves with two nucleation fractions (10^{-2}: solid curves; 10^{-6}: dash curves) are shown for each sandstone. In all three sandstones, water relative permeability curves in the transport-enhanced scenario are much lower compared to those in the diffusion-controlled scenario. Also, the water relative permeabilities in the transport-enhanced scenario drop dramatically with 5–10% gas saturations and drop moderately with further increases in gas saturation. This is caused by preferential gas growth in the pore space with high transport rates in the transport-enhanced scenario, which effectively reduces the water flow with a minimal amount of exsolved gas..

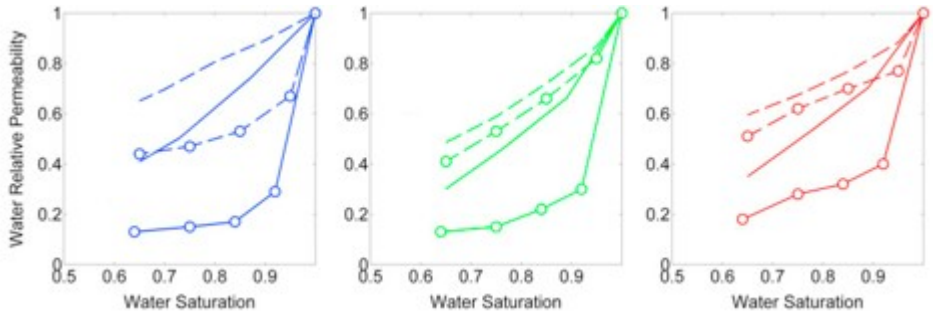

Fig. 19. Comparison of water relative permeability curves in the diffusion-controlled scenario (w/o markers) and the transport-enhanced scenario (w/ markers) with the Domengine (blue), Boise (red) and Berea (green) sandstones. Two nucleation fractions (10^{-2}: solid curves; 10^{-6}: dash curves) are shown.

4.2. Comparison of simulated water relative permeability to core-scale relative permeability measurements

We also measured water relative permeabilities with exsolved CO_2 in larger sandstone cores not amenable to micro-tomography imaging (5 cm in diameter, 10–18 cm in length). Table 1summarizes properties of Berea sandstones used in this study. Each sample is initially saturated with pre-equilibrated carbonated water at 10.34 MPa and 50 °C. Fluids are withdrawn from only one side of the sample until the pore pressure drops to 4.14 MPa. A constant depressurization rate of 1 MPa/h is applied to all samples. Samples 2 and 3 are also measured with 0.1 MPa/h depressurization rate. After exsolved CO_2 is created in the sample, carbonated water (pre-equilibrated at 4.14 MPa) injection is conducted at 2–15 mL/min (Ca=10−7~10−6). The water relative permeability is measured when gas saturation stabilizes, i.e. at the imbibition endpoint.

Table 1. Rock properties and experimental conditions for the comparison between the measured and simulated water relative permeability curves.

Sample	Rock Name	Permeability/mD	Porosity	Diameter, Length/cm
1	Berea	507	19.9	5,14.8

2	Berea	470	19.0	5,16.5
3	Berea	18	16.5	5,17.5

Fig. 20 shows calculated water relative permeability curves and measurements (circles). With a pressure depletion rate between 0.1 and 1 MPa/h, the nucleation fraction is estimated to be approximately 10^{-2}, due to faster depressurization than the experiments with microtomography. The water relative permeability curves shown are calculated in the Berea sandstone digital volume with 10^{-2} nucleation fraction. The measured water relative permeabilities (Samples 1, 2 and 3) are all within the range predicted by the diffusion-controlled and transport-enhanced scenarios, closer to the transport-enhanced curve..

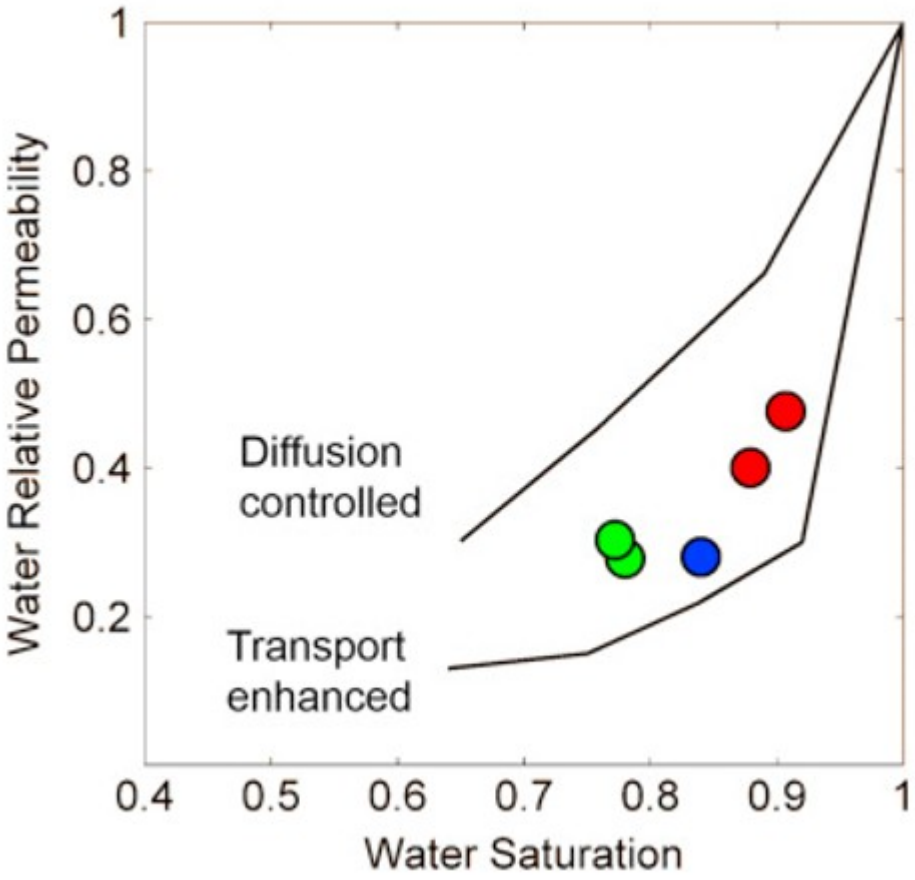

Fig. 20. Comparison of calculated water relative permeability curves with 10^{-2} nucleation fraction in the Berea sandstone sample and measurements (circles) in the core-scale exsolution experiments with Sample 1 (blue), 2 (green), and 3 (red).

5. Discussion and conclusions

We develop a bubble nucleation and growth model with instantaneous nucleation, capillary pressure, and pore geometry constraints. Two scenarios

are considered: a diffusion-controlled scenario, where bubbles grow simultaneously in proportion to their surface area and pore geometry, and a transport-enhanced scenario, where bubble growth is governed by a uniform capillary pressure. However, snap-off mechanism is not modeled. The model only populates gas bubbles in a given porous medium to certain saturations without considering the dynamics of exsolution.

We find that modeling results in the transport-enhanced scenario match the laboratory observation better. At a nucleation fraction of 10^{-3}, the error of modeled ganglion size distribution is 8% in the transport-enhanced scenario and 21% in the diffusion-controlled scenario for the Domengine sandstone, and 13% and 22% for the Boise sandstone (Fig. 14, Fig. 15). Laboratory data also show that exsolved gas is more likely to form and accumulate at locations that have large water flow velocities. These results suggest that convective transfer in the aqueous phase played an important role in bubble growth and accumulation during these experiments. For carbonated brine migrating up a fault from a carbon storagereservoir, the growth of exsolved CO_2 will be largely supported by convection of brine from below.

Water relative permeability with exsolved CO_2 can be simulated with modeled gas distributions under different conditions. The estimated water relative permeability curves in the transport-enhanced scenario agree well with our experimental measurements. According to Tsimpanogiannis and Yortsos (2002), the nucleation fraction is a power law of the depletion rate and the exponent is close to one unless the depletion rate is extremely slow. For carbonated brine migrating up a fault slowly (an equivalent depletion rate of 5 kPa/day), with only 5% exsolved gas, the water relative permeability can be reduced to 0.6~0.8 with various sandstones. Existing GCS reservoir analogs which might benefit from such analysis include the Crystal Geyser site (Paradox Basin, UT) where CO_2 exsolution is known to occur during migration along the Little Grand Wash fault system (Evans et al., 2004, Shipton et al., 2004).

The impact of exsolution on relative permeability appears to increase storage security in geological carbon sequestration. Due to the low mobility of exsolved CO_2 and its large impact on reducing water flow, if carbonated brine migrates upwards and exsolution occurs, brine migration would be limited by the presence of exsolved CO_2 and the consequent low relatively permeability to brine. Similarly, if an exsolved CO_2 phase were to evolve in the seal, for example, after CO_2 injection stops, the effect would be to reduce the permeability to brine and the CO_2 would have very low mobility. However, this phenomenon is dependent on the rate of pressure reduction and nucleation fraction, largely controlled by flow velocity during upward brine migration. This suggests that the initial permeability of the leakage pathway could also impact the relative permeability trajectory during exsolution. In either case, the role of exsolution in controlling relative permeability should be explicitly included when modeling leakage evolution to allow accurate representation of CO_2 mass loss from a storage reservoir.

Acknowledgement

Authors 1 and 5 were funded by the Global Climate and Energy Project (GCEP) at Stanford. Authors 2–4 were supported as part of the Center for Nanoscale Control of Geologic CO_2, an Energy Frontier Research Center funded by the U.S. Department of Energy, under contract number DE-AC02-05CH11231. Micro-tomographic imaging was performed with the assistance of Alastair MacDowell and Dula Parkinson at the Advanced Light Source, Beamline 8.3.2, supported by the U.S. DOE Office of Science, Office of Basic Energy Sciences(DE-AC02-05CH11231). Domengine sandstone samples were kindly provided by Dr. Tim Kneafsey and were obtained with the permission of Black Diamond Regional Preserve, administered by the East Bay Regional Parks District.

Appendix A. Formulation of stokes flow simulator

Formulation of the Stokes flow simulator below is based on the approach taken by Silin and Patzek (2009). Stokes equations for flow of a viscous fluid have the form:

(A.1)∂∂t(ρv)+∇p=μ∇2v

(A.2)∂ρ∂t+∇·(ρv)=0

where v=(vx,vy,vz) is the fluid velocity; p is the fluid pressure; ρ is the fluid density and $\mu$is the fluid viscosity. We assume the Reynolds number, Re=ρVDμ, equals zero for creeping flow.

The artificial compressibility approach developed by Chorin (1967) is utilized to facilitate computations. A linear relationship between the artificial fluid density, ρ, and the pressure, p, is described by the artificial compressibility factor, δ:

(A.3)ρ=δp

such that the pressure and velocity are the only unknowns in Eqs. (A.1), (A.2).

The artificial compressibility factor is optimized for the convergence and stability of iterations. A smaller compressibility should lead to a solution faster but may increase the risk of instability by making the system of equations stiffer. A larger compressibility can slow down the convergence to a steady solution. We use a compressibility factor of 0.1 in results reported here, based on test computations.

Computational domains are digital rock volumes of direct tomography imaging (500×500×500, 4.4 μm voxel size for the Domengine and Boise sandstones, 1.8 μm for the Berea sandstone). The voxels are enumerated by indices i=1,2,…,500, j=1,2,…,500, k=1,2,…,500. Each velocity component is evaluated at the interfaces centers of neighboring voxels. We adopt the convention that the velocity is always associated with the upstream (with respect to the indexing) boundary.

A DuFort-Frankel pattern is employed on a staggered discretization scheme for Eqs. (A.1), (A.2). The DuFort-Frankel pattern is an explicit three-layer scheme and it is known to be unconditionally stable for some classes of boundary-value problems (Samarskii, 2001).

In flow simulations, we let the flow be in the z direction. At the inlet and outlet boundaries (k=1,500), pressures are constant (Dirichlet condition) and only the z velocity components are non-zero. Two artificial slices (k=0,501) are attached to the inlet and outlet to achieve the boundary condition of zero velocity gradient in the z direction (zero Neumann condition). Slice k=0 is identical to k=1, so are slice k=501 to k=500. On the edge boundaries (i,j=1,500), no fluid is allowed to flow in or out of the computational domain, as if the computational domain is wrapped by solid slices i,j=0,501. A no-slip boundary condition is implemented on grain surface inside the computational domain and on the edge boundaries (i,j=1,500).

Let h denote the voxel dimension. The initial pressure of each voxel is given by a constant pressure gradient:

(A.4)pi,j,k=1δ+h(500−k)499

and the initial velocity is given such that the x and y velocity components are zero, and the $z$velocity component is a constant:

(A.5)vz,i,j,k=h24×500

Convergence is determined by calculating the mean square relative increment at each iteration, for example:

(A.6)DVxn=∑i,j,k|vx,i,j,kn−vx,i,j,kn−1|2∑i,j,k(vx,i,j,kn)2

The iterations continue until fulfilling the convergence criterion:

(A.7)max{DVxn,DVyn,DVzn,Dpn}≤ϵtol

where the tolerance, ϵ_{tol}, used in simulations is 10^{-8}. When convergence is achieved, the permeability of the computation domain can be calculated using the average flux of the inlet and outlet and pressure difference between the inlet and outlet.

In calculations of water relative permeabilities with exsolved CO_2, we assume: (1) the rock is water-wet; (2) capillary pressure determines the fluid distribution; (3) exsolved gas is immobile. Zuo et al. (2013) find that a critical gas saturation of 30~35% statistically characterizes when the mobile gas fraction starts to grow in a micromodel. As a result, voxels occupied by exsolved CO_2 are treated as solid grains and no CO_2 movement is allowed when the exsolved CO_2 saturation is less than 35%. Estimates of the water relative permeability are also made between 0~35% gas saturation. Before using the Stokes flow simulator to calculate velocity fields in complex rock geometries, the algorithm was verified with two problems admitting analytical solutions, Poiseuille flow in a pipe and laminar flow around a sphere.

References

Alizadeh et al., 2011

Alizadeh, A.H., Ioannidis, M.A., Piri, M., 2011. CO_2-saturated brine flooding: an effective process for mobilization and recovery of waterflood residual oil. In: International Symposium of the Society of Core Analysts, Austin, Texas, USA.

Al-Raoush and Willson, 2005

R.I. Al-Raoush, C.S. Willson**Extraction of physically realistic pore network properties from three-dimensional synchrotron X-ray microtomography images of unconsolidated porous media systems**

J. Hydrol., 300 (1) (2005), pp. 44-64

Armstrong and Ajo-Franklin,

Armstrong, R., Ajo-Franklin, J.B. Investigating biomineralization using synchrotron based X-ray computed microtomography. Geophysical Research Letters. Vol. 38 (8).

Arora and Kovscek, 2003

P. Arora, A.R. Kovscek**A mechanistic modeling and experimental study of solution gas drive**

Transp. Porous Media, 51 (3) (2003), pp. 237-265

Bachu et al., 1994

S. Bachu, W.D. Gunter, E.H. Perkins**Aquifer disposal of CO_2: hydrodynamic and mineral trapping**

Energy Convers. Manag., 35 (4) (1994), pp. 269-279

Benson et al., 2005

Benson, S.M., P.C. et al., 2005. Underground Geological Storage. IPCC Special Report on Carbon Dioxide Capture and Storage, Chapter 5, Intergovernmental Panel on Climate Change. Cambridge University Press, Cambridge, U.K.

Bondino et al., 2009

I. Bondino, S.R. McDougall, G. Hamon**A pore-scale modelling approach to the interpretation of heavy oil pressure depletion experiments**

J. Pet. Sci. Eng., 65 (1) (2009), pp. 14-22

Bondino,

Bondino, I., McDougall, S.R., Hamon, G. A pore-scale network modeling study of gravitational effects during solution gas drive: Results from macroscale simulations.

Chorin, 1967

A.J. Chorin**A numerical method for solving incompressible viscous ow problems**

J. Comput. Phys., 2 (1967), pp. 12-26

Dong and Blunt, 2009

H. Dong, M.J. Blunt**Pore-network extraction from micro-computerized-tomography images**

Phys. Rev., 80 (3) (2009), p. 036307

Doughty, 2007

C. Doughty**Modeling geologic storage of carbon dioxide: comparison of non-hysteretic and hysteretic characteristic curves**

Energy Convers. Manag., 48 (6) (2007), pp. 1768-1781

Du and Yortsos, 1999

C. Du, Y.C. Yortsos**A numerical study of the critical gas saturation in a porous medium**

Transp. Porous Media, 35 (2) (1999), pp. 205-225

El-Yousfi et al., 1997

El-Yousfi, A., Zarcone, C., Bories, S., 1997. Physical mechanisms for bubble growth during solution gas drive. In: SPE Annual Technical Conference and Exhibition. San Antonio, Texas.

Ennis-King and Paterson, 2005

J. Ennis-King, L. Paterson**Role of convective mixing in the long-term storage of carbon dioxide in deep saline formations**

SPE J., 10 (3) (2005), pp. 349-356

Enouy et al., 2011

R. Enouy, M. Li, M.A. Ioannidis, A. Unger**Gas exsolution and flow during supersaturated water injection in porous media: II. Column experiments and continuum modeling**

Adv. Water Resour., 34 (1) (2011), pp. 15-25

Evans et al., 2004

Evans, J.P., Heath, J., Shipton, Z.K., Kolesar, P.T., Dockrill, B., Williams, A., Kirchner, D., Lachmar, T.E., Nelson, S.T., 2004. Natural leaking CO_2-charged systems as analogs for geologic sequestration sites. In: Proceedings of the Third Annual Conference on Carbon Capture and Sequestration. Alexandria, VA.

Falta et al., 2013

R.W. Falta, L. Zuo, S.M. Benson**Migration of exsolved CO_2 following depressurization of saturated brines**

Greenh. Gases: Sci. Technol., 3 (6) (2013), pp. 503-515

Firoozabadi and Kashchiev, 1996

A. Firoozabadi, D. Kashchiev**Pressure and volume evolution during gas phase formation in solution gas drive process**

SPE J., 1 (3) (1996), pp. 219-223

Fishlock et al., 1988

T.P. Fishlock, R.A. Smith, B.M. Soper, R.W. Wood**Experimental studies on the waterflood residual gas saturation and its production by blowdown**

SPE Reserv. Eng., 3 (2) (1988), pp. 387-394

Fry et al., 1997

V.A. Fry, J.S. Selker, S.M. Gorelick**Experimental investigations for trapping oxygen gas in saturated porous media for in situ bioremediation**

Water Resour. Res., 33 (12) (1997), pp. 2687-2696

Grattoni et al., 1998

Grattoni, C.A., Hawes, R.I., Dawe, R.A., 1998. Relative permeabilities for the production of solution gas from waterflooded residual oil. In: International Symposium of the Society of Core Analysts. The Hague, Netherlands.

Kneafsey et al., 2013

T.J. Kneafsey, D. Silin, J.B. Ajo-Franklin**Supercritical CO_2 flow through a layered silica sand/calcite sand system: experiment and modified maximal inscribed spheres analysis**

Int. J. Greenh. Gas. Control, 14 (2013), pp. 141-150

Landrot et al., 2012

G. Landrot, J.B. Ajo-Franklin, L. Yang, S. Cabrini, C.I. Steefel**Measurement of accessible reactive surface area in a sandstone, with application to CO_2mineralization**

Chem. Geol., 12 (318) (2012), pp. 113-125

Li and Yortsos, 1995

X. Li, Y.C. Yortsos**Theory of multiple bubble growth in porous media by solute diffusion**

Chem. Eng. Sci., 50 (8) (1995), pp. 1247-1271

MacDowell et al., 2012

MacDowell, A.A., Parkinson, D.Y., Haboub, A., Schaible, E., Nasiatka, J.R., Yee, C.A., Jameson, J.R., Ajo-Franklin, J.B., Broderson, C.R., McElrone, A.J., 2012. X-ray micro-tomography at the Advanced Light Source. In: Proceedings SPIE 8506, 8, 5, 0618,

McPherson and Cole, 2000

B.J.O.L. McPherson, B.S. Cole**Transport and sequestration in the powder river basin, Wyoming, U.S.A**

J. Geochem. Explor., 69 (2000), pp. 65-70

Naylor et al., 2000

Naylor, P., Fishlock, T., Mogford, D., Smith, R., 2000. Relative permeability measurements for post-waterflood depressurisation of the Miller field, North Sea. In: SPE Annual Technical and Exhibition. Dallas, Texas, USA.

Noiriel et al., 2012

C. Noiriel, C.I. Steefel, L. Yang, J.B. Ajo-Franklin**Upscaling calcium carbonate precipitation rates from pore to continuum scale**

Chem. Geol., 318 (2012), pp. 60-74

Nordbotten et al., 2008

J.M. Nordbotten, M.A. Celia, H.K. Dahle, S.M. Hassanizadeh**On the definition of macroscale pressure for multiphase flow in porous media**

Water Resour. Res., 44 (2008), p. W06S02

Nyre et al., 2008

Nyre, A.N., McDougall, S.R., Skauge, A., 2008. Effect of depressurization on trapped saturations and fluid flow functions. In: SPE Symposium on Improved Oil Recovery. Tulsa, Oklahoma, USA.

Oldenburg et al., 2012

C.M. Oldenburg, C. Doughty, C. Peters, P. Dobson**Simulations of long-column flow experiments related to geologic carbon sequestration: effects of outer wall boundary condition on upward flow and formation of liquid CO_2**

Greenh. Gases: Sci. Technol., 2 (4) (2012), pp. 279-303

Paganin et al., 2002

D. Paganin, S. Mayo, T. Gureyev, P. Miller, S. Wilkins**Simultaneous phase and amplitude extraction from a single defocused image of a homogeneous object**

J. Microsc., 206 (1) (2002), pp. 33-40

Perkins et al., 2005

Perkins, E., Czernichowski-Lauriol, I., Azaroual, M. Durst, P., 2005. Long term predictions of CO_2 storage by mineral and solubility trapping in the Weyburn Midale reservoir. In: Proceedings of the 7th InternationalConference on Greenhouse Gas Control Technologies, Volume II. Elsevier, Oxford, pp. 2093–2096.

Poulsen et al.,

Poulsen, S., McDougall, S., Sorbie, K., Skauge, A. Network modelling of internal and external gas drive 17.

Pruess and Garcia, 2002

K. Pruess, J. Garcia**Multiphase flow dynamics during CO_2 disposal into saline aquifers**

Environ. Geol., 42 (2–3) (2002), pp. 282-295

Pruess, 2005

Pruess, K., 2005. ECO2N: A TOUGH2 fluid property module for mixtures of water, NaCl, and CO_2. Lawrence Berkeley National Laboratory Report. LBNL–57952.

Riaz et al., 2006

A. Riaz, M.A. Hesse, H.A. Tchelepi, F. Orr**Onset of convection in a gravitationally unstable diffusive boundary layer in porous media**

J. Fluid Mech., 548 (2006), pp. 87-111

Samarskii, 2001

A.A. Samarskii**The Theory of Difference Schemes**

M. Decker, New York, U.S.A (2001)

Satic et al., 1995

C. Satic, X. Li, Y.C. Yortsos**Scaling of single-bubble growth in a porous medium**

Phys. Rev. E (Stat. Phys., Plasmas, Fluids, Relat. Interdiscip. Top.), 51 (4) (1995), pp. 3286-3295

Scriven, 1959

L.E. Scriven**On the dynamics of phase growth**

Chem. Eng. Sci., 10 (1–2) (1959), pp. 1-13

Shipton et al., 2004

Shipton, Z.K., Evans, J.P., Kirschner, D., Kolesar, P.T., Williams, A.P., Heath, J., 2004. Analysis of CO_2 leakage through-low-permeability faults from natural reservoirs in the Colorado Plateau, east-central Utah. Geological Society, London, Special Publications. Vol. 233 (1), pp. 43–58.

Silin and Patzek, 2006

D. Silin, T. Patzek**Pore space morphology analysis using maximal inscribed spheres**

Physica A: Stat. Mech. its Appl., 371 (2) (2006), pp. 336-360

Silin and Patzek, 2009

Silin, D., Patzek, T., 2009. Predicting relative-permeability curves directly from rock images. In: SPE Annual Technical Conference and Exhibition. New Orleans, LA, USA.

Tang and Firoozabadi, 2003

G.Q. Tang, A. Firoozabadi**Gas- and liquid-phase relative permeabilities for cold production from heavy oil reservoir**

SPE Reserv. Eval. Eng., 6 (2) (2003), pp. 70-80

Tanino and Blunt, 2012

Y. Tanino, M.J. Blunt**Capillary trapping in sandstones and carbonates: dependence on pore structure**

Water Resour. Res., 48 (8) (2012), p. W08525

Tsimpanogiannis and Yortsos, 2002

I.N. Tsimpanogiannis, Y.C. Yortsos**Model for the gas evolution in a porous medium driven by solute diffusion**

AIChE J., 48 (11) (2002), pp. 2690-2710

Weitkamp et al., 2011

T. Weitkamp, D. Haas, D. Wegrzynek, A. Rack**ANKAphase: software for single-distance phase retrieval from inline X-ray phase contrast radiographs**

J. Synchrotron Radiat., 18 (4) (2011), pp. 617-629

Wilt, 1986

P.M. Wilt**Nucleation rates and bubble stability in water carbon dioxide solutions**

J. Colloid Interface Sci., 112 (2) (1986), pp. 530-538

Wu et al., 2011

Y. Wu, J. Ajo-Franklin, N. Spycher, S.S. Hubbard, G. Zhang, K.H. Williams, J. Taylor, Y. Fujita, R.Smith**Geophysical monitoring and reactive transport modeling of ureolytically-driven calcium carbonate precipitation**

Geochem. Trans., 12 (7) (2011), pp. 1-20

Yortsos and Parlar, 1989

Yortsos, Y.C., Parlar, M., 1989. Phase change in binary systems in porous media: application to solution-gas drive. In: SPE Annual Technical Conference and Exhibition, San Antonio, TX.

Zhao and Ioannidis, 2011

W. Zhao, M.A. Ioannidis**Gas exsolution and flow during supersaturated water injection in porous media: I. Pore network modeling**

Adv. Water Resour., 34 (1) (2011), pp. 2-14

Zuo and Benson, 2013

L. Zuo, S.M. Benson**Exsolution enhanced oil recovery with concurrent CO_2 sequestration**

Energy Procedia, 37 (2013), pp. 6957-6963

Zuo et al., 2012

L. Zuo, S.C.M. Krevor, R.W. Falta, S.M. Benson**An experimental study of CO_2 exsolution and relative permeability measurements during CO_2saturated water depressurization**

Transp. Porous Media, 91 (2) (2012), pp. 459-478

Zuo et al., 2013

L. Zuo, C. Zhang, R.W. Falta, S.M. Benson**Micromodel investigations of CO_2 exsolution from carbonated water in sedimentary rocks**

Adv. Water Resour., 53 (2013), pp. 188-197